Composites Science and Technology 256 (2024) 110772

Contents lists available at ScienceDirect

Composites Science and Technology

journal homepage: www.elsevier.com/locate/compscitech

A statistical volume element-based procedure for the prediction of the mechanical and electrical response of an epoxy-PZT self-sensing layer for application in composite laminates

Michele Gulino [a,*], Andrea Zucchelli [b], Alessandro Pirondi [a], Tommaso Brugo [b]

[a] Department of Engineering for Industrial Systems and Technologies, University of Parma, Parco Area delle Scienze 181/A, 43124, Parma, Italy
[b] Department of Industrial Engineering, Alma Mater Studiorum - University of Bologna, Viale del Risorgimento 2, 40136, Bologna, Italy

ARTICLE INFO

Handling editor: Ming-Qiu Zhang

Keywords:
Statistical volume element
FEM
SHM
Lead zirconate titanate
Homogenized properties

ABSTRACT

Structural Health Monitoring (SHM) techniques are being developed to continuously oversee defects in composite structures. Within this context, research is focusing on the development of new types of sensors with high sensitivity and proper integration in the laminate.

In this work, the mechanical and electrical properties of a recently developed piezoelectric composite material made of a Lead Zirconate Titanate (PZT) powder embedded in an epoxy matrix are evaluated with finite element simulations of plane strain Statistical Volume Elements (SVEs). The homogenized properties are then implemented in a second finite element model of a composite specimen with the embedded self-sensing material and loaded in compression. The electrical sensitivity is evaluated as a function of the distance between the signal electrodes.

The results show that the finite element models with the homogenized properties have decreasing sensitivity with increasing electrodes distance, in agreement with the experimental results from another work, in which Glass Fiber Reinforced Polymer (GFRP) laminates with the embedded piezoelectric composite are loaded in compression and tested for output signal.

1. Introduction

Composite materials play a dominant role in the manufacturing of lightweight structures as the limits on energy consumption and pollutants emissions are becoming more and more stringent. Among them, long fiber-reinforced polymers have high stiffness and strength-to-weight ratio, but their laminated structure makes them inherently weak to out-of-plane loadings and prone to delamination. Moreover, interlaminar defects usually initiate and propagate without any visible recognition, leading to sudden catastrophic failure. In this context, research has been focusing on the development of Non-destructive testing (NDT) techniques which can be used for the characterization and localization of internal defects in composite structures, such as thermography [1], X-ray Computed Tomografy (X-ray CT) [2] and Acoustic Emissions (AE) [3] among others.

Structural Health Monitoring (SHM) techniques are also used to assess the presence of defects in a structure in real time and evaluate the propagation of such defects, to estimate its remaining service life. SHM has been widely applied in many fields, such as aerospace and civil engineering, to replace scheduled maintenance with as-needed maintenance for existing structures, thus avoiding the cost of periodic NDT [4–11]. Moreover, SHM allows for a less conservative and damage tolerant design of new structures, which is of paramount importance in many fields (e.g., aerospace) to reduce weight and energy consumption.

SHM methods can be classified as passive or active based on the type of sensors involved in the monitoring process. In the former, the sensors can only detect defects based on how the structure responds to an external perturbation, such as operational loading or impacts. Some examples of passive SHM sensors are optical fibers [12], AE sensors [13] and strain gauges [14]. In active systems, on the other hand, the structure is equipped with actuators that produce a perturbation themselves (usually in the form of vibrations) and sensors that can evaluate the structure's response to such loading. Piezoelectric materials are an example of sensors/actuators used in active SHM systems [15].

In the context of composite laminates, SHM sensors can either be externally attached or embedded in the composite. The first ones do not

* Corresponding author.
E-mail address: michele.gulino@unipr.it (M. Gulino).

https://doi.org/10.1016/j.compscitech.2024.110772
Received 17 April 2024; Received in revised form 1 July 2024; Accepted 18 July 2024
Available online 19 July 2024

usually affect the laminate properties but are exposed to environmental hazard, such as impacts and electrical interference [16]. For the second type of sensors, Fiber Bragg Grating (FBG) [17,18] and ceramic piezoelectric transducers [19] are commonly used. The integration in the lamination process eliminates the typical drawbacks of the external sensors, but can be detrimental for the laminate properties in terms of impact resistance. Thus, the research is moving towards the improvement of the integration of the embedded monitoring sensors.

Carbon Nanotubes (CNTs) have been exploited not only to increase the mechanical properties of composite laminates [20], but also for piezoresistive monitoring via making the composite's matrix electrically conductive [21,22]. While the CNTs can be perfectly integrated in the composite, the main drawback is the incapability of damage localization, in contrast to piezoelectric based sensors.

In the work of Brugo et al. [23], a mat of piezoelectric Poly (vinylidenefluoride-trifluoroethylene) (PVDF-TrFE) electrospun nanofiber was interleaved in a Glass Laminate Aluminum Reinforced Epoxy (GLARE), using the aluminum sheets as electrodes, and overcoming the issues related to the integration of a bulk sensor in the laminate while still being capable of detecting impacts. Similarly, in the work of Selleri et al. [24] the same type of nanostructured PVDF-TrFE mat was interleaved in a fiber reinforced laminate with polymeric electrodes mixed with carbon black nanoparticles. The resulting self-sensing material was able to detect impact loading and non-impulse loading. Also, the polymeric electrodes showed great integration in the laminate, avoiding the material discontinuity that the introduction of metal electrodes could have caused.

Ceramic piezoelectric SHM sensors, like Lead Zirconate Titanate (PZT) sensors, usually have high sensitivity, but are inherently brittle. To overcome this issue, composite PZT-resin materials have been studied to combine high piezoelectric constants with higher toughness compared to the bulk ceramic material [25]. This new type of PZT-resin composites would improve the integration of embedded piezoelectric ceramics inside composite laminates, especially for the localization of impact events, which requires multiple sensors.

An interesting solution for the integration of embedded piezoelectric ceramic sensors in a composite laminate is the manufacture of micrometric PZT powder. While the concept of using a PZT powder can be found in the literature for the development of sensors and paints [26–31], their integration in a composite laminate needs further investigation.

In the investigation carried by Gino et al. [32], a commercial PZT disk was ground to obtain a micrometric powder which was embedded in a Glass fiber laminate with brass sheet electrodes. The powder was embedded in the laminate prior to curing, and the system was polarized by applying an electric field of 4 kV/mm to the brass electrodes. The impact tests and the micrographic analysis showed a higher sensitivity and a much better integration of the powder sensors compared to the samples with bulk PZT disks. Moreover, the authors developed an analytical model of the electrical circuit to predict the sensitivity of the samples as a function of the volumetric fraction of the powder and the distance between the signal electrodes.

To the authors knowledge, a micromechanical simulation of a PZT powder-epoxy resin composite is lacking in the literature. The micromechanical simulation can be used to predict both the mechanical behavior and the sensitivity in terms of electrical field vs. stress of such a system starting from commercial PZT disks and polymer properties.

The simulation route drawn in this work takes the sensors manufactured by Gino et al. [32] as a reference for the development of FE Statistical Volume Elements (SVEs) of the PZT-epoxy composite, to give a detailed evaluation of its homogenized mechanical, dielectric, and piezoelectric properties for application in design and digital twinning of self-sensing composite structures. Indeed, the route can be applied not only to composite laminates but also, for instance, to adhesive joints.

This possibility would open new promising scenarios for the design of self-sensing composite laminates or bonded joints with an excellent integration between the sensor and the host structure which would have significant potential for engineering applications.

Validation of the proposed route has been done using homogenized properties to simulate the experiments done by Gino et al. [32], showing good agreement between the two.

Table 1
Sample naming and corresponding electrodes distance.

	electrodes distance [mm]
COM	0.38
P2400-G8	2.42
P2400-G4	1.44
P2400-G2	1.08

2. Notation adopted in this work

Two-dimensional axisymmetric or plane strain finite element models have been developed in this work using the software ABAQUS® version 2021. For these models, ABAQUS requires that the reference coordinate system for the material orientation has the revolution axis in the 2 (Y) direction. This means that, referring to the figures of the FE models in this work, the 3 (Z) direction is perpendicular to the cross section of the samples, while 1 and 2 directions are in the plane of the cross-section. Since the usual notation for piezoelectric materials prescribes the index 3 to the polarization direction, the material properties and the results are presented to this standard. For the coordinate transformation of the material properties, please refer to the appendix to this paper.

From now on, the polarization direction will be referred to as the 3 direction in a cartesian coordinate system, thus the d_{333} constant stands for the proportionality between the applied electric field and the resulting deformation in the mentioned direction. Also, for the sake of clarity, a contracted notation is enforced, where 11->1, 22->2, 33->3, 12->4, 13->5, 23->6. For instance, the d_{333} constant will be referred as to d_{33} henceforth. For further clarification on the piezoelectric behavior, please refer to the appendix of this paper.

3. Experiments

In this work, two different types of laminates are investigated among the ones manufactured in the study by Gino et al. [32], namely.

- A conventional self-sensing GFRP laminate with a BB-35-3L0 PZT commercial sensor from Murata in its midplane (hereafter called COM), comprising of the built-in signal electrodes.
- Three GFRP laminates with the PZT powder in their midplanes, hereafter called PWD. The powder was distributed with an areal density of 2400 g/m^2. Circular brass sheets were used as signal electrodes (20 mm diameter and 0.1 mm thickness and 30 mm diameter with 0.1 mm thickness for the top and the bottom electrodes respectively). The electrodes are positioned during the lamination at a different distance depending on the sample, i.e. with 2 (sample P2400-G2), 4 (sample P2400-G4) or 8 (sample P2400-G8) GFRP plies between them, according to Table 1 and Fig. 1.

In both the COM and the PWD laminates, all the plies have the same orientation. The laminates have a square shape with a 50 mm side length.

In order to model the geometry of the SVEs, an additional PWD sample is manufactured and cut in its mid-plane. The sample is then polished and a micrograph of the cross-section is taken with a Axio Observe A1 microscope (Zeiss, Oberkochen, Germany). The geometry of the SVEs is then modeled from the micrograph as will be described in *Section 4.2.1. SVE models setup*.

A summary of the materials, manufacturing technology, polarization process and mechanical testing of these samples done by Gino et al. [32]

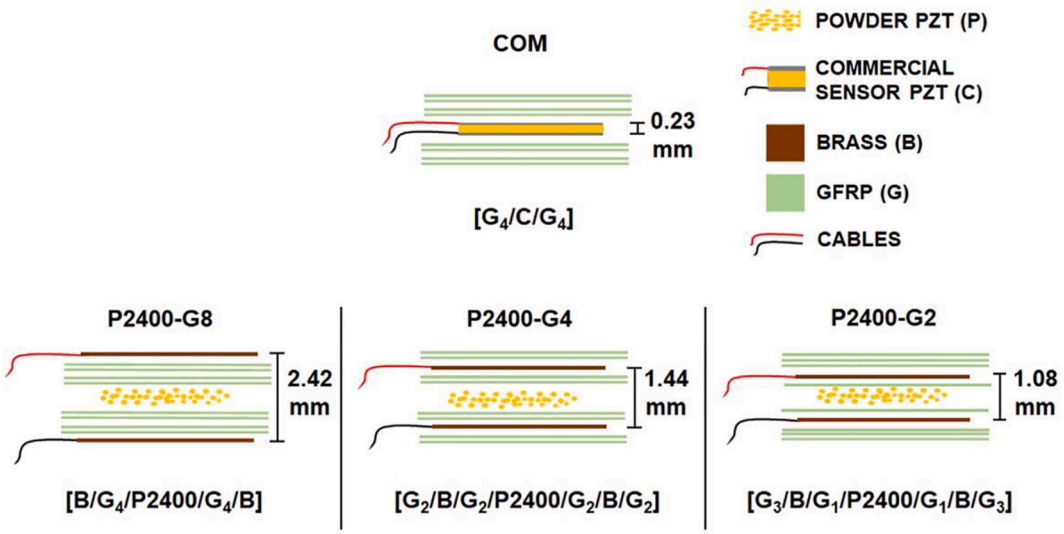

Fig. 1. Samples with stacking sequence.

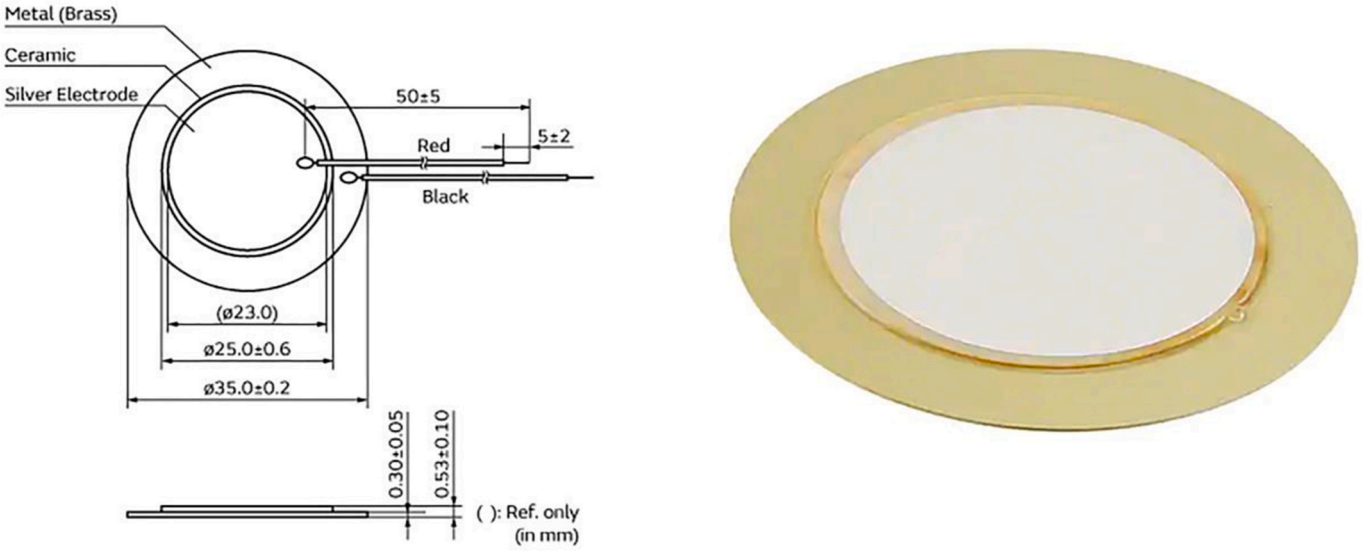

Fig. 2. Schematics and dimensions of the Piezotite P–7B piezoelectric disk commercial sensor from Murata, with picture on the right. The upper electrode is silver coating (~0 mm thickness), while the lower electrode is brass. All dimensions in millimetres.

is reported in the following.

3.1. Materials and manufacturing of the samples

In the work of Gino et al. [32], the PZT powder was derived from a Murata BB-35-3L0 commercial sensor, consisting of a Piezotite P–7B piezoelectric disk with a metallized silver coating and a glued brass sheet as electrodes (Fig. 2).

To obtain the powder, the PZT disk was first detached from the brass electrode via thermal treatment at 350 °C for 1 h, which also depolarizes the piezoelectric material (the PZT disk's Curie temperature is 300 °C, which is less than the 350 °C of the treatment).

After detaching the electrode, the PZT disk was ground with a rotating blade mill (IKA A 10 basic) at 25 000 rpm for 20 s. The PZT powder was then uniformly spread over the first half of the uncured laminate using a circular mask with a 20 mm diameter.

The epoxy matrix of the GFRP prepreg (E-glass 8H Satin 300 g/m^2, epoxy matrix, VV300S - DT121H-34 Delta-Preg, 50x50 × 0.245 mm^3) impregnated the PZT powder during the cure cycle, without additional resin.

Brass electrodes were introduced in the stacking sequence of the PWD samples, in order to capture the electric charge from the sensing layer. A total of 9 PWD samples were manufactured, varying both the number of GFRP plies between the electrodes (2, 4 and 8 plies) and the PZT powder areal density (600 g/m^2, 1200 g/m^2 and 2400 g/m^2), to assess the effect of these two parameters on the sensitivity. As stated at the beginning of *Section 3. Experiments*, only the PWD samples with 2400 g/m^2 areal density were examined in this study, since they were the ones with the highest sensitivity. Nevertheless, the methodology used in this work can be readily extended to samples with different PZT

Table 2
material properties. Subscripts (a), (d), and (e) stand for "assumed", "datasheet" and "experimental" respectively. For the mechanical properties of the PZT, ***D*** is the compliance tensor, thus D_{ij} are its terms in contracted notation.

GFRP			PZT		
E_1 (a)	[MPa]	23600	D_{11} (d)	[MPa]	140967.0
E_2 (a)	[MPa]	22300	D_{12} (d)	[MPa]	80361.0
E_3 (a)	[MPa]	8000	D_{13} (d)	[MPa]	80483.0
G_{12} (a)	[MPa]	22890	D_{33} (d)	[MPa]	128463.0
G_{13} (a)	[MPa]	2000	S_{44} (d)	[MPa]	29412.0
G_{23} (a)	[MPa]	2000	S_{66} (d)	[MPa]	30303.0
ν_{12} (a)	[−]	0.1	κ_1^{rel} @20°C (a)	[−]	1825.2
ν_{13} (a)	[−]	0.3	κ_2^{rel} @20°C (a)	[−]	0.0
ν_{23} (a)	[−]	0.3	κ_3^{rel} @20°C (e)	[−]	1801.0
κ_1^{rel} @20°C (a)	[−]	7	κ_1 @20°C (a)	[F/mm 10^{-15}]	16150.9
κ_2^{rel} @20°C (a)	[−]	7	κ_2 @20°C (a)	[F/mm 10^{-15}]	0.0
κ_3^{rel} @20°C (e)	[−]	7	κ_3 @20°C (e)	[F/mm 10^{-15}]	15937.0
κ_1 @20°C (a)	[F/mm 10^{-15}]	58	d_{33}^{eq} (e)	[mm/V 10^{-9}]	450.0
κ_2 @20°C (a)	[F/mm 10^{-15}]	58	d_{33} (d)	[mm/V 10^{-9}]	271.0
κ_3 @20°C (e)	[F/mm 10^{-15}]	58	d_{31} (d)	[mm/V 10^{-9}]	−131.0
κ_1^{rel} @100°C (a)	[−]	7	d_{15} (d)	[mm/V 10^{-9}]	400.0
κ_2^{rel} @100°C (a)	[−]	7	γ @20°C (e)	[S/mm 10^{-18}]	223
κ_3^{rel} @100°C (e)	[−]	7	γ @100°C (e)	[S/mm 10^{-18}]	2600
κ_1 @100°C (a)	[F/mm 10^{-15}]	60			
κ_2 @100°C (a)	[F/mm 10^{-15}]	60			
κ_3 @100°C (e)	[F/mm 10^{-15}]	60			
γ @20°C (e)	[S/mm 10^{-18}]	4			
γ @100°C (e)	[S/mm 10^{-18}]	143			

powder densities.

For the manufacturing of the COM sample, the commercial PZT sensor from Murata was embedded in the GFRP laminate with its own electrodes. All the samples were cured in an autoclave at a pressure of 6 bar with the vacuum bag technique and a three-step curing cycle, namely 30 min at 50 °C, 120 min at 100 °C and 60 min at 150 °C, with 2 °C/min heating ramps.

3.2. Polarization

From now on, the superscripts *P*, *G*, *R* and *C* are used when referring to physical quantities regarding the PZT, the GFRP, the GFRP matrix resin and the whole composite laminate, respectively.

Bulk PZT disks were then polarized at 100 °C for 24 h, with different electric field intensities to check the influence on the d_{33} piezoelectric deformation constant. The experimental data were then interpolated with the following formula [32]:

$$d_{33} = a\left(1 - e^{-b\Psi_3^P}\right) - c \tag{1}$$

Where *a*, *b* and *c* are fitting coefficients (614 p.m./V, 2.19 mm/kV, and 143 p.m./V respectively [32]), and Ψ_3^P is the electric field applied at the PZT electrodes. Eq (1) shows that d_{33} reaches a stable value of 450 p.m./V for applied electric fields Ψ of 2 kV/mm or higher. The PZT disks were also tested for electrical permittivity and conductivity at both 20 °C and 100 °C. The properties of the PZT are shown in Table 2 together with those of the GFRP.

In the COM laminate, the polarization field was applied evenly at the boundaries of the PZT disk. In the PWD laminates, on the other hand, the field distributed unevenly over the GFRP and the PZT-resin phases, according to the polarization model developed by Gino et al. [32]:

$$\Psi^P = \frac{\frac{\Psi_3^C}{\gamma^P}}{\frac{V_f^P}{\gamma^P} + \frac{1-V_f^P}{\gamma^G}} \tag{2}$$

which gives the electric polarization field on the PZT particles (Ψ^P). Ψ_3^C is again the electric field, applied in this case to the laminate's electrodes, while γ and V_f are the conductivities and volumetric fraction of the phases, respectively. Superscript *P* refers to the PZT and superscript *G* to the GFRP.

In order to reach the saturation value of d_{33}, according to Eq. (1), the electric field applied for polarization was 4 kV/mm at 100 °C (below the glass transition temperature of the resin) for 24 h for both COM and PWD samples.

3.3. Mechanical testing

The samples were tested with a cyclic compressive load between 0.5

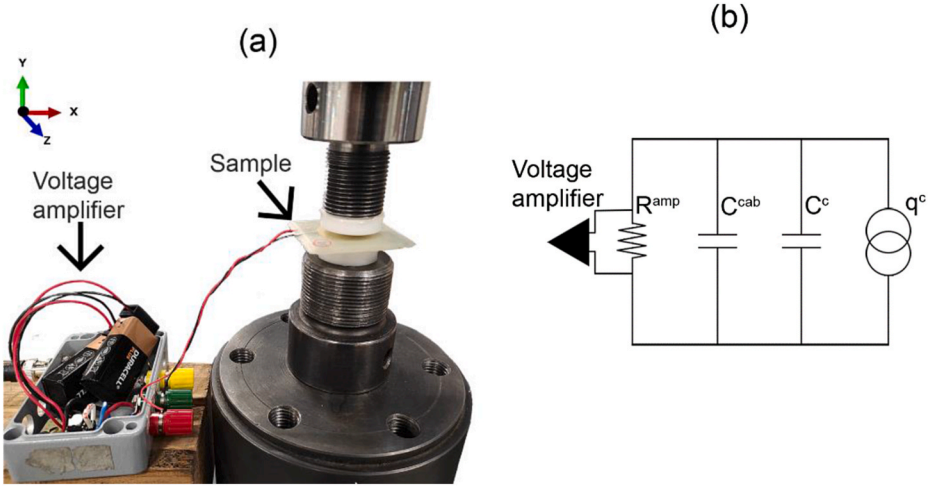

Fig. 3. (a) Experimental setup and (b) electric circuit of the piezoelectric sample, that can be modeled as a charge generator q^c in parallel with its capacitance C^c, where the superscript C stands for the sensing composite laminate. C^{cab} is the cables' capacitance and R^{amp} is the resistance of the amplifier.

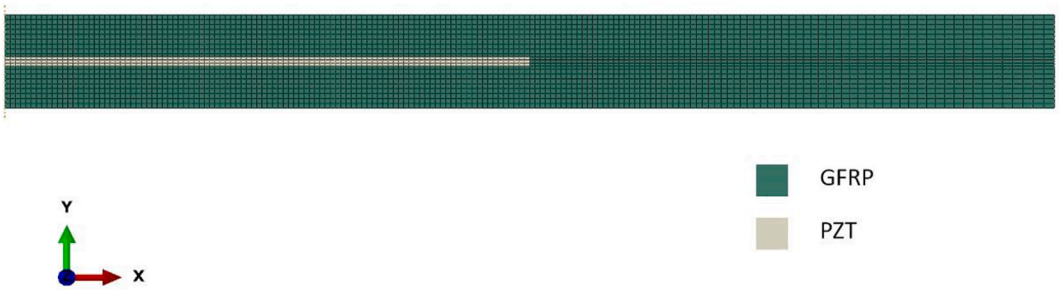

Fig. 4. Surface of revolution of the axisymmetric FE model with quadrilateral element meshing. In this model, the 2 axis (Y in the model triad) is the direction of polarization, load application and stacking sequence.

and 1 kN at 25 Hz in an Instron 8033 hydraulic testing machine equipped with PolyOxyMethylene (POM) indenters (10 mm in diameter for the upper and 30 mm for the lower) and a dedicated signal amplifier (Texas Instruments INA118, Dallas, Texas, U.S.A.), as shown in Fig. 3.

4. Modeling methodology

4.1. COM sensing laminate model

The first step of the work is the setup of a coupled electrical-mechanical FE model of the COM sensing laminate with the commercial software ABAQUS, as a guideline to validate the FE simulations of the PWD samples.

Given the circular shape of both the commercial sensor and the brass electrodes, an axisymmetric model is chosen to represent the sample (Fig. 4). The whole model is discretized with first-order quadrilateral piezoelectric elements, which have 3 degrees of freedom, namely the in-plane displacements and the electric potential.

The GFRP plies are treated with a macromechanical approach, i.e., as a homogenous medium defined by orthotropic elasticity and null piezoelectric constants. The PZT disk (0.23 mm thickness, 25 mm of diameter) is characterized with transversely isotropic elasticity with the dielectric and piezoelectric constants shown in Table 2.

The loading setup is simulated with a 1000 N downward concentrated force applied to the uppermost node of the axis of symmetry. The POM upper indenter is modeled by constraining the vertical displacement d.o.f. of the adjacent nodes within 5 mm (radius of the upper indenter) from the axis of symmetry to be equal to the loaded node. The bottom plastic support is modeled as an analytical rigid axisymmetric surface in contact with the sample with a 0.2 coefficient of friction, which is chosen to be plausible for the case study.

For the COM sample, the upper electrode is silver metallized (~0 mm thickness), while the bottom electrode is a circular brass sheet of 0.3 mm thickness, resulting in an averaged electrode distance of 0.38 mm (0.23 + 0 + 0.3/2 mm). The upper electrode is therefore modeled as an equipotential surface imposing the same electric potential of a reference node for all the nodes at a vertical distance of (0.38–0.23)/2 from the upper edge of the PZT disk. The same procedure is followed for the bottom electrode, where all the nodes are set to be at null electric potential (Figs. 5 and 6). The electric potential used for the evaluation of the sample sensitivity was taken from the reference node of the upper electrode.

To evaluate the sensitivity of the COM sample, the voltage output between the two electrodes resulting from a given load is needed. Being the bottom electrode at null electrical potential, plotting the electric potential for the upper reference node gives the voltage across the electrodes, namely 2.29 V. Dividing the voltage by the applied load of 1000 N gives a sensitivity of 2.29 V/kN which is close to the experimental value of 2.31 V/kN [32], with a difference of less than 1 %.

Since this axisymmetric modeling approach worked well for the COM sample, it will be applied later to the simulation of PWD samples modeled with the homogenized properties coming from the micromechanical analysis.

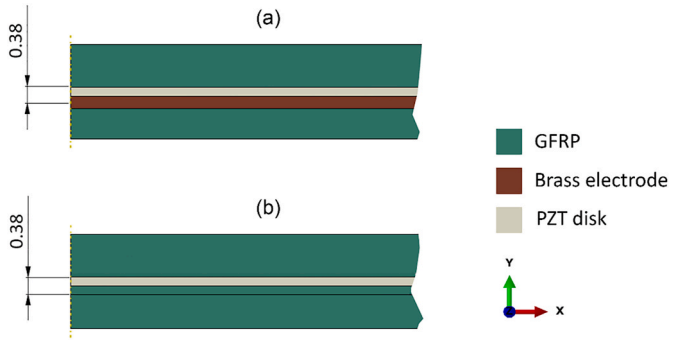

Fig. 5. (a) brass electrode (the silver electrode is not represented as it has negligible thickness); (b) approximation of the electrodes as two partition lines at a distance of 0.38 mm, i.e. the mean distance from the brass electrode and the upper disk surface (silver electrode). The partition lines are then used to enforce the equipotential constraint.

4.2. FE simulations of the SVEs

4.2.1. Clarification on the use of Statistical Volume Elements (SVEs)

The properties homogenization of heterogenous materials such as composites is usually associated to the concept of Representative

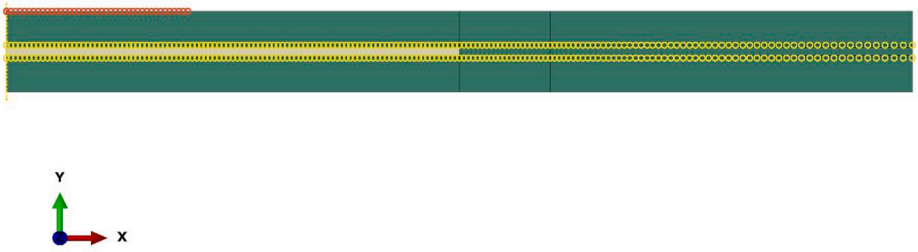

Fig. 6. Modeling of the electrodes as equipotential nodes (yellow circles). The red circles are the node bound to have the same vertical displacement.

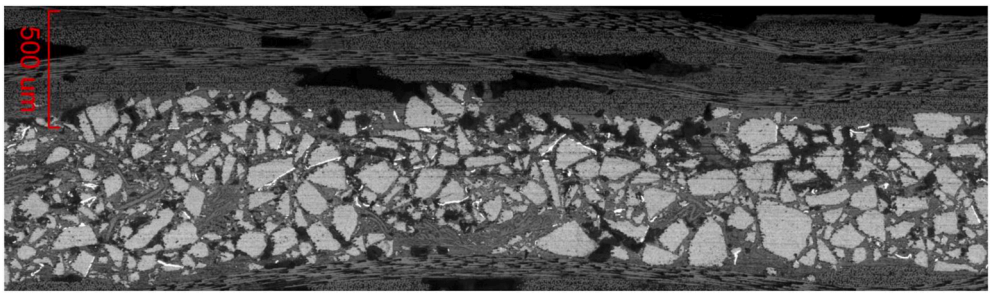

Fig. 7. Optical micrograph of the PZT-epoxy composite.

Volume Element (RVE) [33–37], i.e. a material point that is representative of its whole structure. The RVE (mesoscale) acts as the connection between the microscale, which is the scale of the reinforcement (PZT particles in this case) and the macroscale, namely the scale of the macroscopic component (in this case the PZT enriched resin layer). These conditions imply that the RVE has a size large enough to contain a population of particles such that the mesoscale properties are no longer dependent on particle size and distribution. In this work instead, there is not a strong dimensional separation between the macroscale and the microscale and, therefore, it is not possible to identify a region in the PZT-enriched resin layer which is truly representative of the whole material. Therefore, it is more appropriate to use the concept of Statistical Volume Element (SVE) [38,39], i.e. a material point that takes into account the variability in the microstructure using multiple realizations, each one differing from the other in terms of yielded results, over which the homogenized material properties are averaged.

4.2.2. SVE models setup

The PZT-epoxy composite under examination has a powder distribution as shown in Fig. 7. The image is an optical micrograph of a radial section enclosing the epoxy-PZT layer captured with a Axio Observe A1 microscope (Zeiss, Oberkochen, Germany).

The powder-interleaved area of the laminate has a maximum thickness of approximately 765 μm near the center of the circular patch, gradually decreasing to 363 μm towards the extremities.

The PZT areal density is approximately 2400 g/m^2, given by 0.75 g of powder spread over a circular patch of 0.02 m of diameter i.e. 3.14*10^{-4} m^2 area. An average thickness of 579 μm, is probed along 37 points from the optical micrograph image, resulting in a volume of the region with PZT powders of 1.82*10^{-7} m^3, thus a powder volumetric density of 4120 g/m^3.

Square images of the optical microscopy are sampled for the numerical analysis (Fig. 8); image sizes of 0.15 x 0.15, 0.3 x 0.3 and 0.5 × 0.5 mm^2, are considered to appraise the effect of different SVE's dimensions on the output results. Four images are sampled in different positions of the micrograph for each size of SVE.

The results of the SVEs of the different samples are then averaged size by size, in order to smooth possible differences related to the local particle distribution.

The 2D sketches are filled with a quad-dominated mesh. Plane strain piezoelectric first-order elements having an average element size of 167 μm are used, after a convergence study on the strain energy of the models. The choice of a 2D model is related to the availability of just 2D pictures of the microstructure in a radial section; this of course is a limitation of the model with respect to a full 3D representation, that on the other hand would require either a time-consuming sectioning or a tomography. When dealing with a 2D model, the option of a plane strain model over an axisymmetric one was driven by the fact that, in the latter, the circumferential and radial deformations depend on the distance from the axis of symmetry, i.e. the homogenized properties are dependent on the positioning of the SVE in the FE model. Preliminary simulations were made with a SVE at a distance of 5 mm from the axis of symmetry (halfway between the axis and the outer radius of the powder patch), leading to results similar to the ones obtained with the plane strain model (<1 % difference in sensitivity between the plane strain and axisymmetric models for all the SVE dimensions), therefore plane strain assumption is considered reasonable in this case.

Periodic boundary conditions are implemented via a Python code

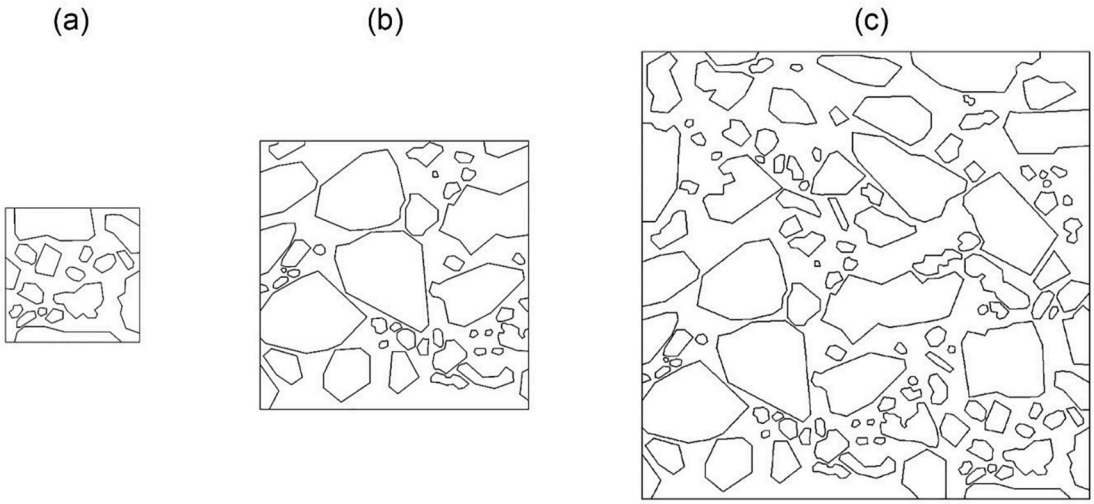

Fig. 8. Sketches of the three different SVE sizes: (a) 0.15 mm, (b) 0.3 mm, (c) 0.5 mm. The composite material is sampled 4 times for each SVE size to average the results of the homogenization. The images are then imported in a CAD software (SolidWorks) as a guideline to draw the geometry for the SVE model. The sketches are saved with a.dxf extension and imported in ABAQUS for the finite element analysis.

Table 3
Piezoelectric and dielectric properties of the two phases. Superscript P stands for powder while R stands for resin.

	g_{33}^{P}	d_{33}^{P}	κ_{33}^{P}	d_{33}^{R}	κ_{33}^{R}
	[Vm/N]	[m/V]	[F/m]	[m/V]	[F/m]
P2400-G8	6.90E-03	1.10E-10	1.59E-08	0	6.20E-11
P2400-G4	8.30E-03	1.32E-10	1.59E-08	0	6.20E-11
P2400-G2	1.10E-02	1.75E-10	1.59E-08	0	6.20E-11

that constrains all the pairs of homologous nodes on the top and bottom edges and left and right edges to have the same difference in displacements of the nodes on the corners.

In absence of data about the permittivity of the epoxy matrix, it is assumed to be equal to that of the GFRP plies, while the elastic modulus and the Poisson's coefficient are assumed to be 2750 MPa and 0.38 respectively, that are reasonable values for an epoxy [40].

For the PZT powder particles, the dielectric and elastic constants are taken from the experiments of Gino et al. [32] and the datasheet respectively. The piezoelectric constant, on the other hand, is chosen depending on the number of plies interposed between the electrodes in the PWD samples: the higher the number of plies, the lower the polarization electric field applied to the PZT particles, hence the lower the resulting piezoelectric constant.

Knowing the volumetric fraction of the powder for the considered samples, the resulting piezoelectric constants, which are presented in Table 3, can be calculated as:

$$d_{33}^{P} = g_{33}^{P}\kappa_{33}^{P} \tag{3}$$

Where g_{33}^{P} and κ_{33}^{P} are respectively the piezoelectric stress and dielectric constants of the PZT powder in the polarization direction.

4.3. Homogenized properties definition

4.3.1. Mechanical properties

For given stress and strain fields, the average stresses and strains in the chosen SVE of material can be defined as:

$$\overline{\sigma}_{ij} = \frac{1}{V}\int_{V}\sigma_{ij}dV \tag{4}$$

$$\overline{\varepsilon}_{ij} = \frac{1}{V}\int_{V}\varepsilon_{ij}dV \tag{5}$$

Where V is the volume of the SVE.

The homogenized mechanical properties of the material are calculated assuming that the average deformation is equal to the applied constant deformation at the boundaries, and similarly for the stress [33–37]:

$$\varepsilon_{ij}^{0} = \overline{\varepsilon}_{ij} \tag{6}$$

$$\sigma_{ij}^{0} = \overline{\sigma}_{ij} \tag{7}$$

Where ε_{ij}^{0} and σ_{ij}^{0} are constant strains and stresses over the boundary of the SVE, obtained by imposing displacements $u_i(B)$ (Dirichlet boundary conditions) or tractions $t_i(B)$ (Neumann boundary conditions), respectively, such that at the boundary:

$$u_i(B) = \varepsilon_{ij}^{0}x_j \tag{8}$$

$$t_i(B) = \sigma_{ij}^{0}n_j \tag{9}$$

Where x_j and n_j are, respectively, the spatial coordinates and the components of the unit outward normal vector of the SVE's boundary B.

Therefore, the effective elastic moduli are evaluated as relations between the average stresses and strains:

$$\overline{\sigma}_{ij} = D_{ijkl}\overline{\varepsilon}_{kl} \tag{10}$$

Hereafter, for the sake of conciseness, the superscript bar on average strains and stresses is omitted.

Two different assumptions are made about the epoxy-PZT composite's mechanical properties: 1) the composite material is isotropic, 2) the composite material is transversely isotropic. If the resulting material is isotropic, then the constitutive equations can be written in Voigt's notations:

$$\begin{bmatrix}\varepsilon_1\\ \varepsilon_2\\ \varepsilon_3\\ \varepsilon_4\\ \varepsilon_5\\ \varepsilon_6\end{bmatrix} = \begin{bmatrix} {}^{1}/_{E} & -{}^{\nu}/_{E} & -{}^{\nu}/_{E} & 0 & 0 & 0\\ -{}^{\nu}/_{E} & {}^{1}/_{E} & -{}^{\nu}/_{E} & 0 & 0 & 0\\ -{}^{\nu}/_{E} & -{}^{\nu}/_{E} & {}^{1}/_{E} & 0 & 0 & 0\\ 0 & 0 & 0 & {}^{1}/_{G} & 0 & 0\\ 0 & 0 & 0 & 0 & {}^{1}/_{G} & 0\\ 0 & 0 & 0 & 0 & 0 & {}^{1}/_{G}\end{bmatrix}\begin{bmatrix}\sigma_1\\ \sigma_2\\ \sigma_3\\ \sigma_4\\ \sigma_5\\ \sigma_6\end{bmatrix} \tag{11}$$

Which, for a plane strain scenario ($\varepsilon_2 = \varepsilon_4 = \varepsilon_6 = 0$), yield the following system of equations:

$$\varepsilon_1 = \frac{\sigma_1}{E} - \frac{\nu}{E}(\sigma_2 + \sigma_3) \tag{12}$$

$$0 = \frac{\sigma_2}{E} - \frac{\nu}{E}(\sigma_1 + \sigma_3) \tag{13}$$

$$\varepsilon_3 = \frac{\sigma_3}{E} - \frac{\nu}{E}(\sigma_1 + \sigma_2) \tag{14}$$

$$\varepsilon_5 = \sigma_5/G \tag{15}$$

The Poisson's coefficient can be calculated from Eq. (13) as:

$$\nu = \frac{\sigma_2}{\sigma_1 + \sigma_3} \tag{16}$$

While (12) and (14) yield the Young's modulus:

$$E = \frac{\sigma_3}{\varepsilon_3} - \frac{\sigma_2(\sigma_1 + \sigma_2)}{\varepsilon_3(\sigma_1 + \sigma_3)} \tag{17}$$

If the material is transversely isotropic, then, from Eq. (18) with $D_{13} = D_{23}, D_{11} = D_{22}$:

$$\begin{bmatrix}\sigma_1\\ \sigma_2\\ \sigma_3\\ \sigma_4\\ \sigma_5\\ \sigma_6\end{bmatrix} = \begin{bmatrix} D_{11} & D_{12} & D_{13} & 0 & 0 & 0\\ D_{21} & D_{22} & D_{23} & 0 & 0 & 0\\ D_{31} & D_{32} & D_{33} & 0 & 0 & 0\\ 0 & 0 & 0 & D_{44} & 0 & 0\\ 0 & 0 & 0 & 0 & D_{55} & 0\\ 0 & 0 & 0 & 0 & 0 & D_{66}\end{bmatrix}\begin{bmatrix}\varepsilon_1\\ \varepsilon_2\\ \varepsilon_3\\ \varepsilon_4\\ \varepsilon_5\\ \varepsilon_6\end{bmatrix} \tag{18}$$

$$\sigma_1 = D_{11}\varepsilon_1 + D_{13}\varepsilon_3 \tag{19}$$

$$\sigma_2 = D_{12}\varepsilon_1 + D_{13}\varepsilon_3 \tag{20}$$

$$\sigma_3 = D_{13}\varepsilon_1 + D_{33}\varepsilon_3 \tag{21}$$

$$\sigma_5 = D_{55}\varepsilon_5 \tag{22}$$

and by introducing $D_{13} = D_{12}$, $D_{11} = D_{22}$, then:

$$D_{11} = D_{22} = \frac{\sigma_1}{\varepsilon_1} - \frac{\sigma_2}{\varepsilon_1 + \varepsilon_3}\varepsilon_3 \tag{23}$$

$$D_{33} = \frac{\sigma_3}{\varepsilon_3} - \frac{\sigma_2}{\varepsilon_1 + \varepsilon_3}\frac{\varepsilon_1}{\varepsilon_3} \tag{24}$$

$$D_{13} = D_{23} = D_{12} = \frac{\sigma_2}{\varepsilon_1 + \varepsilon_3} \tag{25}$$

Table 4
Homogeneous Dirichlet boundary conditions for the determination of the elastic moduli. "u_1, u_2, u_3" are the displacements, ϕ is the electric potential. "l" is the size of the SVE.

	Applied boundary conditions
E,ν,D$_{11}$,D$_{13}$	$u_1(x=0)=0$ $u_1(x=l)=\varepsilon^0_{11}l$ $u_3(z=0;z=l)=0$ $\phi(B)=0$
D$_{33}$	$u_1(x=0;x=l)=0$ $u_3(z=0)=0$ $u_3(z=l)=\varepsilon^0_{33}l$ $\phi(B)=0$
D$_{55}$	$u_1(x=0)=0$ $u_3(x=0)=0$ $u_3(x=l)=0$ $u_1(x=l)=\frac{1}{2}\gamma^0_{13}l$ $\phi(B)=0$

$$D_{55}=\sigma_5/\varepsilon_5 \tag{26}$$

Three different models with different loading and boundary conditions are created for the constants to be determined, namely one for the assessment of E, ν, D_{11} and D_{13}, one for the D_{33} modulus and the last one for the D_{55} modulus (Table 4, Fig. 9).

While both Neumann and Dirichlet boundary conditions should be considered for the evaluation of homogenized mechanical properties, only the results obtained with the latter are shown in this work for the sake of clarity and conciseness, since in a preliminary study no significant differences in the homogenized properties were recorded between the two cases (Table 5).

It is worth noting that across the three examined dimensions, a decreasing trend in the Young's modulus difference can be observed with increasing SVE size (Table 5). Nevertheless, given the small number of samples and the limited maximum size of the SVE, the trend is not monotonic, with the minimum difference in Young's modulus given for the SVE with 0.3 mm size.

Table 6
Homogeneous boundary conditions for the determination of the dielectric constants.

	Applied boundary conditions
κ_1	$u_1(x=0;x=l)=0$ $u_3(z=0;z=l)=0$ $\phi(x=l)=\phi_0$
κ_3	$u_1(x=0;x=l)=0$ $u_3(z=0;z=l)=0$ $\phi(z=l)=\phi_0$

4.3.2. Dielectric properties

For the assessment of the dielectric properties, an energetic approach is followed [41–44]:

$$U_D=\frac{1}{2}\kappa_{ij}\Psi_i\Psi_j \tag{27}$$

where U_D is the electrostatic energy of the system, while κ_{ij} , Ψ_i , Ψ_j are the components of the permittivity and electric field respectively.

As for the traction and displacement, the electric potential ϕ at the boundary of the SVE is chosen to be homogeneous, via the implementation of the periodic boundary conditions as explained in *Section 4.2.1. SVE models setup:*

$$\phi(B)=-\Psi^0_i x_i \tag{28}$$

Since the permittivity of the bulk PZT is transversely isotropic, the epoxy-PZT composite is assumed to behave in the same way i.e., in a matrix notation:

$$\boldsymbol{\kappa}=\begin{bmatrix}\kappa_1 & 0 & 0\\ 0 & \kappa_2 & 0\\ 0 & 0 & \kappa_3\end{bmatrix};\kappa_1=\kappa_2 \tag{29}$$

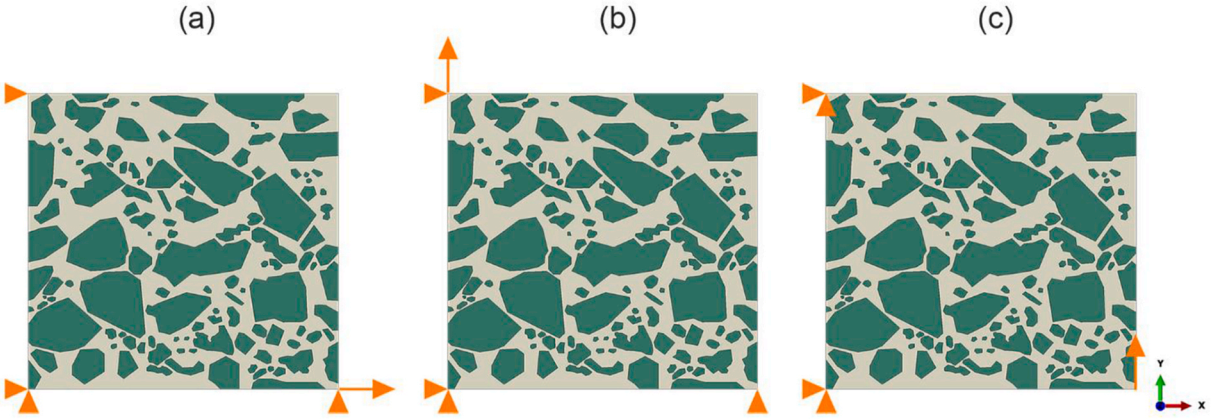

Fig. 9. Boundary conditions for the evaluation of (a) E, ν, D_{11}, D_{13} (b), D_{33} and (c) D_{55}. The PZT phase is shown in green while the resin matrix is shown in grey. The orange triangles are hinges while the orange arrows are imposed displacements.

Table 5
Preliminary study on the Young's modulus of the PZT-resin composite obtained with Dirichlet's and Neumann's boundary conditions, showing only minor differences between the two approaches.

SVE size [mm]	G8			G4			G2		
	$E_{dirichlet}$	$E_{neumann}$	|diff%|	$E_{dirichlet}$	$E_{neumann}$	|diff%|	$E_{dirichlet}$	$E_{neumann}$	|diff%|
	[Mpa]		[%]	[Mpa]		[%]	[Mpa]		[%]
0.15	10 598	11 274	6.386	10 610	11 291	6.412	10 639	11 328	6.473
0.3	10 279	10 276	0.030	10 285	10 282	0.030	10 298	10 295	0.030
0.5	9682	9422	2.683	9689	9429	2.683	9705	9445	2.683

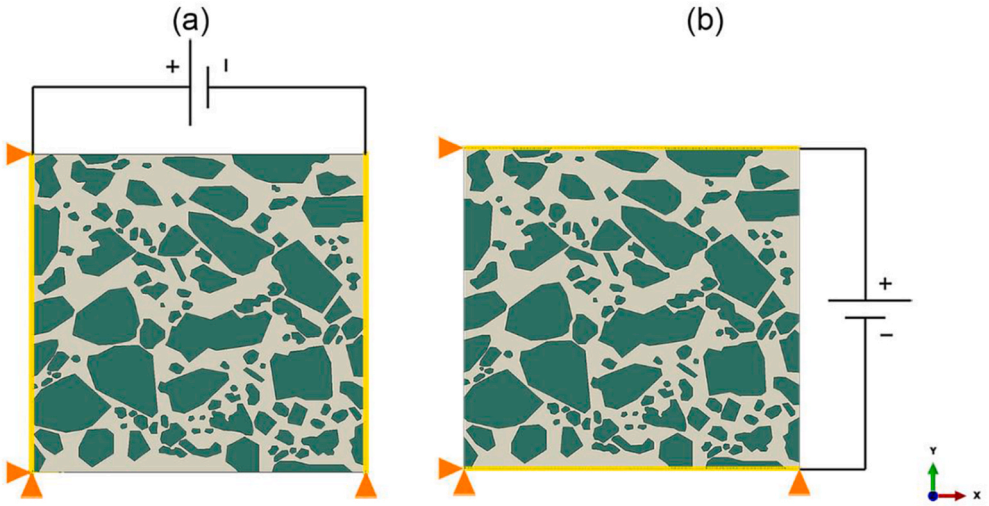

Fig. 10. Boundary conditions for the evaluation of (a) κ_1, with null electric potential at the left edge and 1 V at the right edge, and (b) κ_2, with null electric potential at the bottom and 1 V at the top edge.

Thus, in the model used to determine κ_3, the applied electric potential is null at the bottom edge and 1 V at the top edge. For the κ_1 constant, the electric potential is null at the left edge and one at the right edge (Table 6, Fig. 10).

4.3.3. Piezoelectric properties

The piezoelectric properties are determined based on the average deformation caused by the applied electric field e.g.: for a unit cell of 0.5 mm side, with a difference of potential between the top and bottom edges of 1 V, the electric field is 1/0.5 = 2 V/mm. Knowing this value, the piezoelectric deformation constant can be calculated as:

$$d_{33} = \varepsilon_3 / \Psi_3 \tag{30}$$

The boundary conditions applied for the determination of d_{33} are the same as the ones for the determination of κ_2 (Fig. 10, Table 7).

Table 7
Homogeneous boundary conditions for the determination of the d_{33} constant.

	Applied boundary conditions
d_{33}	$u_1(x = 0; x = l) = 0$ $u_3(z = 0; z = l) = 0$ $\phi(z = l) = \phi_0$

5. Results and discussions

5.1. Homogenized properties

The formulas for the evaluation of the homogenized properties are applied to each SVE model, and the results are averaged over the 4 sampled microstructures for the $l = 0.15$, 0.3 mm and 0.5 mm side size SVE.

The homogenized properties are listed in Tables 8 and 9, where the results are presented for all the three different sizes of SVE.

The values of d_{33}, E and κ_3^{rel} are shown against the distance between the electrodes in Fig. 11 and against the SVE size in Fig. 12.

The values of mechanical properties are almost independent of the electrodes distance as expected, while the choice of the SVE size has a limited impact on them (±5 % around the average of the three SVEs). Concerning the permittivity κ, the values are also independent from the electrodes distance, while the dependence on the SVE size is higher than that of mechanical properties (±10 % around the average of the three SVE), though still quite limited. The piezoelectric constant d_{33} instead, exhibits an expected dependence on the electrodes distance that is related to the polarization process, where the larger the distance, the lower the polarization electrical field applied on the powders. However, it shows also a fairly large dependence on the SVE size (±22 % around the average of the three SVE), hence for this property the homogenization process might necessitate a further refinement in future.

Table 8
Homogenized properties for each model and SVE dimension.

		SVE 0.15 mm			SVE 0.3 mm			SVE 0.5 mm		
		P2400-G8	P2400-G4	P2400-G2	P2400-G8	P2400-G4	P2400-G2	P2400-G8	P2400-G4	P2400-G2
E	[MPa]	10597.7	10610.4	10639.3	10278.8	10284.9	10298.4	9681.6	9688.9	9705.4
ν	[−]	0.343	0.343	0.343	0.342	0.342	0.342	0.344	0.344	0.344
D_{11}	[MPa]	15370.8	15368.6	15363.8	16418.7	16416.7	16412.5	14920.2	14918.2	14913.6
D_{33}	[MPa]	14153.3	14210.0	14337.2	13202.6	13243.9	13335.9	13695.1	13743.8	13852.6
D_{13}	[MPa]	7892.9	7888.9	7879.9	8635.8	8632.7	8625.9	7776.2	7772.8	7765.1
D_{55}	[MPa]	3123.9	3124.7	3126.3	3243.3	3243.8	3245.1	3377.9	3378.8	3381.1
d_{33}	[mm/V]	2.73E-09	3.17E-09	3.90E-09	1.80E-09	2.09E-09	2.55E-09	2.44E-09	2.83E-09	3.48E-09
κ_3	[F/mm]	3.18E-10	3.18E-10	3.20E-10	2.63E-10	2.63E-10	2.64E-10	3.01E-10	3.02E-10	3.03E-10
κ_1	[F/mm]	4.67E-10	4.67E-10	4.67E-10	4.43E-10	4.43E-10	4.44E-10	3.70E-10	3.70E-10	3.71E-10
κ_3^{rel}	[−]	35.92	35.98	36.11	29.74	29.77	29.83	34.04	34.09	34.20
κ_1^{rel}	[−]	52.73	52.74	52.77	50.06	50.08	50.14	41.85	41.86	41.90

Table 9
Average and standard deviation of homogenized properties for SVE of same dimension.

		SVE 0.15 mm		SVE 0.3 mm		SVE 0.5 mm	
		Average	Std.dev.	Average	Std.dev.	Average	Std.dev.
E	[MPa]	10615.8	17.4	10287.4	8.2	9692.0	10.0
ν	[−]	0.343	6.3E-06	0.342	3.322E-06	0.344	4.773E-06
$\mathbf{D_{11}}$	[MPa]	15367.7	2.9	16416.0	2.6	14917.4	2.8
$\mathbf{D_{33}}$	[MPa]	14233.5	76.9	13260.8	55.7	13763.8	65.8
$\mathbf{D_{13}}$	[MPa]	7887.2	5.4	8631.4	4.1	7771.4	4.6
$\mathbf{D_{55}}$	[MPa]	3125.0	1.0	3244.1	0.8	3379.3	1.3
$\mathbf{d_{33}}$	[mm/V]	3.269E-09	4.803E-10	2.145E-09	3.092E-10	2.916E-09	4.296E-10
$\boldsymbol{\kappa_3}$	[F/mm]	3.186E-10	6.92E-13	2.635E-10	3.072E-13	3.019E-10	5.931E-13
$\boldsymbol{\kappa_1}$	[F/mm]	4.668E-10	1.437E-13	4.433E-10	2.842E-13	3.705E-10	1.767E-13
$\boldsymbol{\kappa_3^{rel}}$	[−]	36.00	0.08	29.78	0.0347153	34.11	0.07
$\boldsymbol{\kappa_1^{rel}}$	[−]	52.75	0.02	50.09	0.0321168	41.87	0.02

5.2. Validation of the homogenized properties on PWD experiments

The homogenized properties are then introduced in the compression loaded sensing laminate modeled in *Section 4.1. COM sensing laminate model*, with, in this case, the electrodes at different distances according to Table 1, (3 models, namely P2400-G8, P2400-G4 and P2400 -G2). A total of six simulations are made for each model, one for every SVE size and their corresponding properties, both with the isotropic and transversely isotropic behavior.

The results for the sensitivity are listed in Table 10 and plotted against the electrodes distance in Fig. 13.

The results of the FE simulations show a trend of decreasing sensitivity for increasing electrodes distance in accordance with the experiments, since 1) as the electrodes are moved further apart from the PZT-powder patch, it can be assumed that the electrical charges reaching them are lowered and 2) during the polarization process, the lower the distance between the electrodes, the higher the electric field inside the PZT layer, leading to higher piezoelectric constants [32]. A difference in the steepness of the curve must be noted though, with the experimental curve having a more abrupt increase of sensitivity with the reduction of

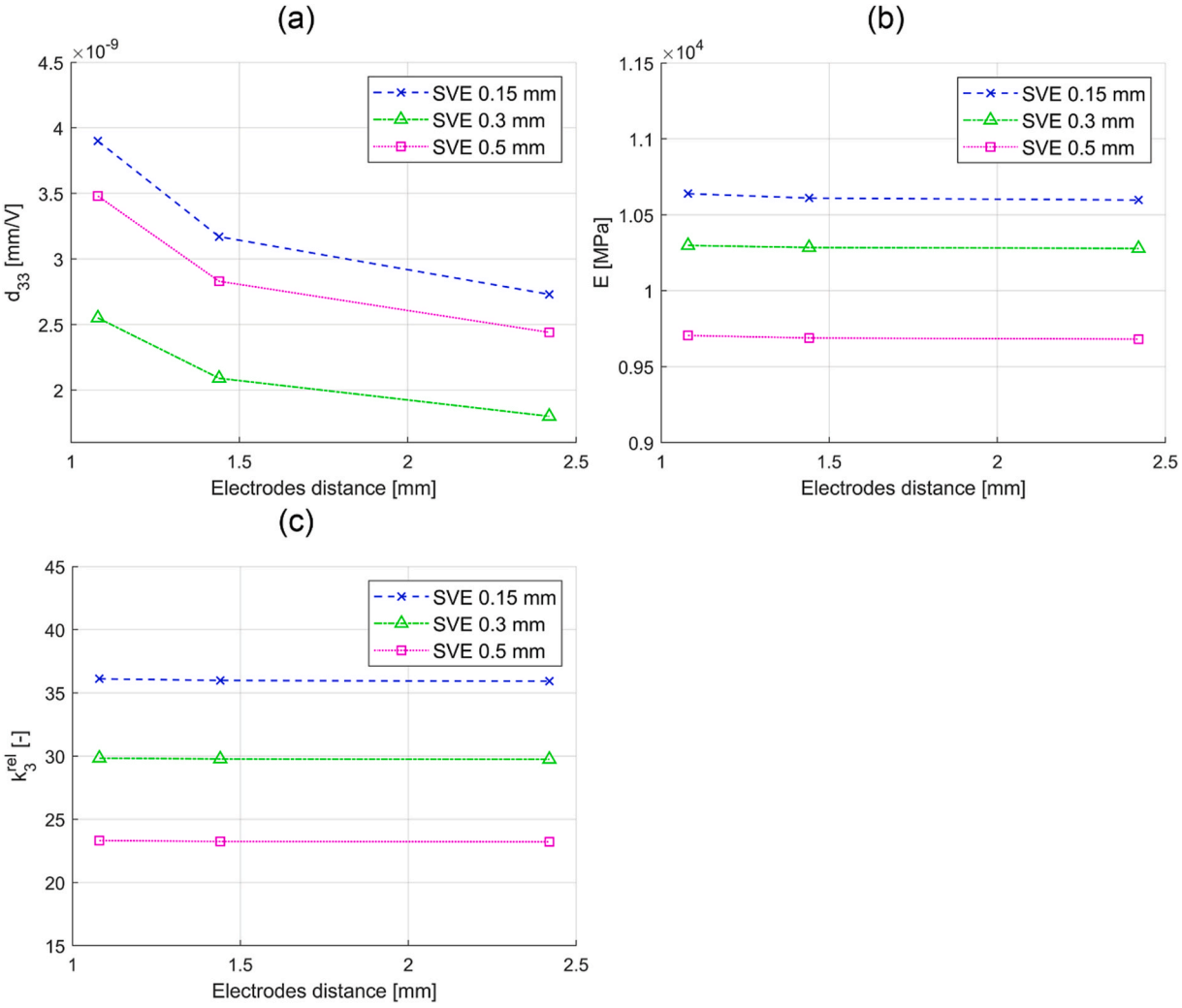

Fig. 11. Trend of (a) d_{33}, (b) E and (c) κ_3^{rel} against the distance between the electrodes.

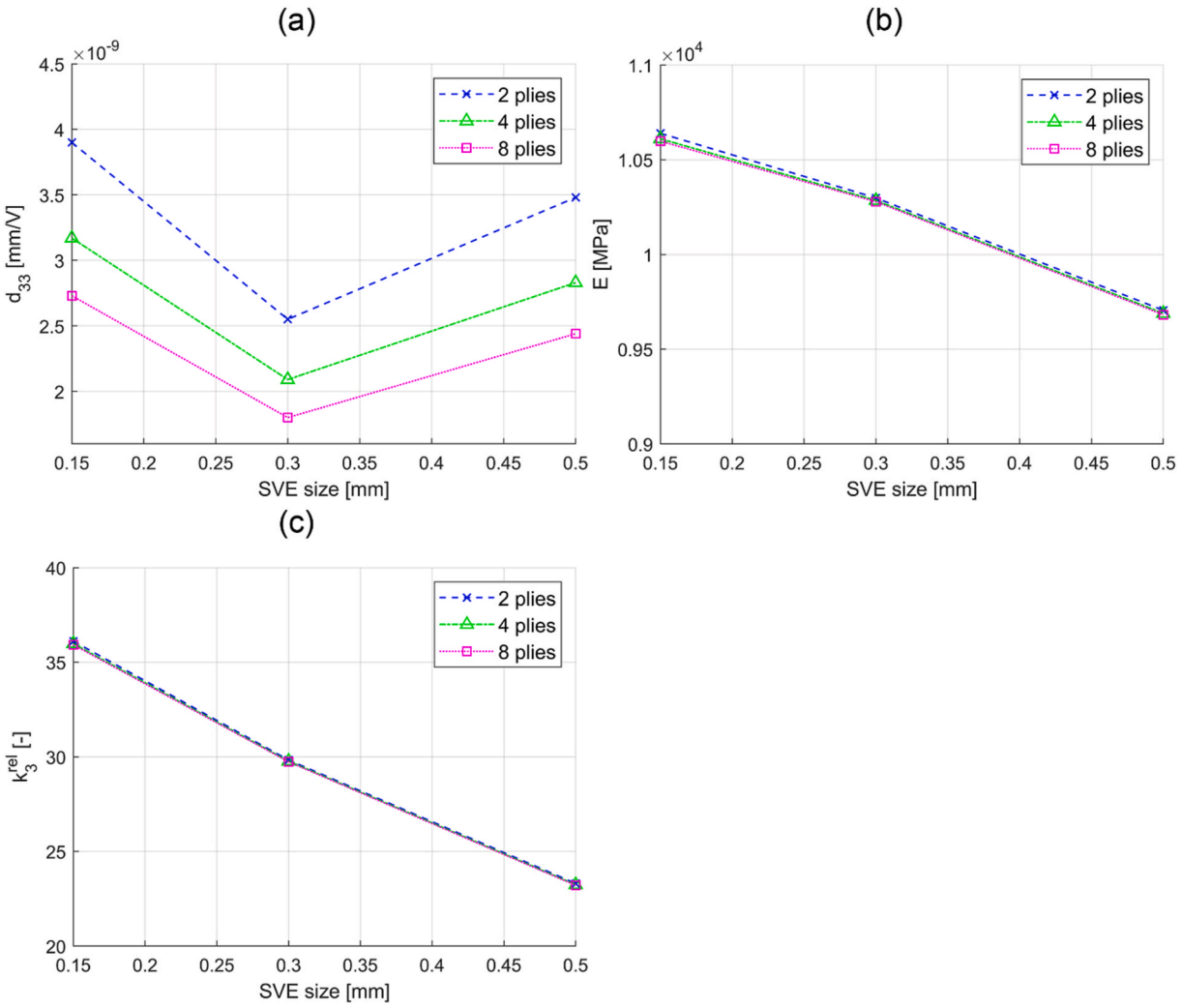

Fig. 12. Trend of (a) d_{33}, (b) E and (c) κ_3^{rel} against the size of the SVE.

Table 10
Comparison of the sensitivity from experiments and FE models. "ISO" and "TR_ISO" stand for isotropic and transversely isotropic, respectively.

	Sensitivity [mV/kN]					
	ISO	TR_ISO	ISO	TR_ISO	ISO	TR_ISO
	P2400-G8		P2400-G4		P2400-G2	
Experimental	3620		8600		12 440	
SVE 0.15 mm	4247.0	4247.0	6054.2	6054.3	9098.0	9098.6
SVE 0.3 mm	3340.9	3341.4	4695.2	4695.8	6892.5	6894.1
SVE 0.5 mm	3995.8	3996.0	5651.5	5651.7	8470.8	8471.4

the electrodes distance. The P2400-G8 sample behavior was accurately captured from all the models, while the difference from the experimental results is more marked for the other two samples. The models with the homogenized properties derived from the 0.15 mm side SVE show an overall better fit compared to the other two.

For all the samples, the difference of the sensitivity for the models with isotropic and orthotropic elasticity is negligible.

The differences in the output sensitivity are probably due to three factors, namely.

- the proportion between the micro, meso and macro scale of the samples, meaning that the thickness of the powder-resin phase (macro-scale) is comparable to the dimension of the powder (micro-

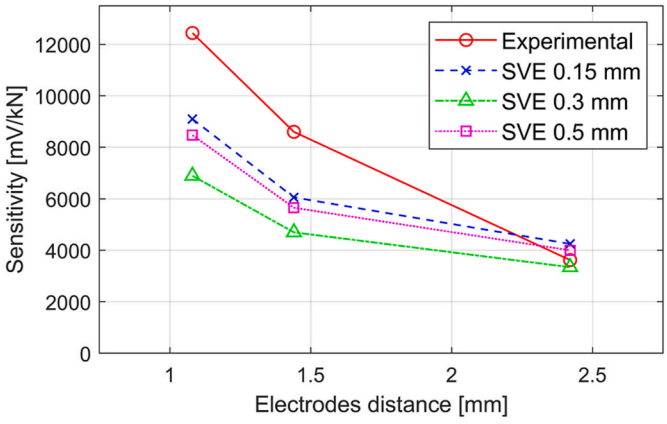

Fig. 13. Plot of the sensitivity against the electrodes distance. The continuous line is the experimental result, while the dashed lines are the numerical results. For the sake of clarity, only the results for the transversely isotropic homogenized properties are presented, as the differences from the isotropic models are negligible.

scale), leaving little room for the definition of the SVE's characteristic dimension (meso-scale).
- The lenticular shape of both the electrodes and the powder patch due to the autoclave curing, which was not considered in the FE model and could potentially lead to variations in the relative distance between the two, hence non-homogeneous polarization electric field. The difference between real and nominal distance between the electrodes due to their curvature is more marked for samples P2400-G2 and P2400-G4 compared to sample P2400-G8, which is likely the reason why the sensitivity of the latter is better represented by the SVE models.
- The fact that a possible influence of the polarization field on the dielectric properties was not taken into consideration.

5.3. Evaluation of d_{31} and d_{15} piezoelectric constants

The experimentally retrieved d_{33}, incorporates the effect of deformation. Specifically, since the powder patch is embedded in the GFRP, and since the indenter and the support have different diameters, non-negligible strains in the radial directions arise (Fig. 14), which must be coupled with the electric field generated in the axial direction. The contribution of d_{31} can reduce the measured d_{33} by up to a factor of 3 depending on the tested PZT family and the loading condition [45,46].

To account for this effect, the FE models should be populated with all the piezoelectric constants, namely d_{31} and d_{15}. Assuming that the ratios between the d_{33} and the other deformation constants are the same as the ones in the Murata commercial disk datasheet:

$$d_{33}^{d} \Big/ d_{31}^{d} = -2.069; \;\; d_{33}^{d} \Big/ d_{15}^{d} = 0.678 \tag{31}$$

Where the superscript d stands for "datasheet".

Considering the homogenized properties coming from the 0.15 mm side SVE, which showed the best overall match with the experimental data, the same type of FE models of *Section 4.1*. *COM sensing laminate model* is run adding the d_{31} and d_{15} calculated from the ratios showed in Eq. (31). The resulting sensitivity is higher than the one coming from the model with just d_{33}, because the d_{31} contributes to the overall electric

Table 11
Equivalent d_{33} vs. complete piezoelectric characterization (d_{33}, d_{31}, d_{15}).

		P2400-G8	P2400-G4	P2400-G2
$\mathbf{d_{33}^{eq}}$	**[mm/V]**	2.73E-09	3.17E-09	3.90E-09
$\mathbf{d_{33}^{fe}}$	**[mm/V]**	3.73E-09	4.33E-09	5.32E-09
$\mathbf{d_{31}^{fe}}$	**[mm/V]**	−1.80E-09	−2.09E-08	−2.57E-09
$\mathbf{d_{15}^{fe}}$	**[mm/V]**	5.50E-09	6.39E-09	7.85E-09

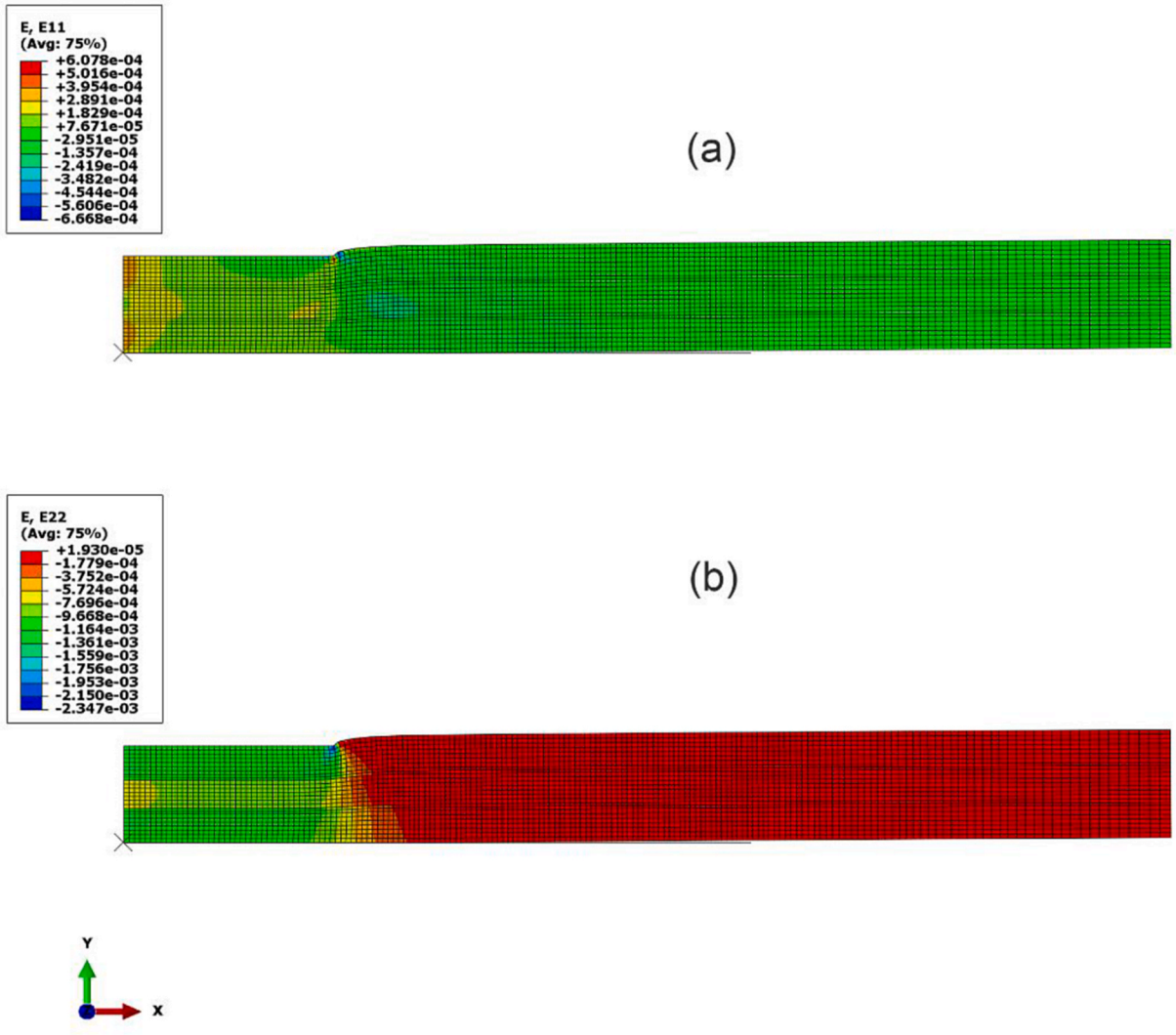

Fig. 14. Non negligible strains in the radial direction (b) compared to the axial direction (a). Applied load is 1000 N in compression. The deformation scale is set at 100x.

Table 12
Homogenized properties comprising d_{31} and d_{15} for the best fitting model (SVE 0.15 mm).

		Homogenized properties		
		P2400-G8	P2400-G4	P2400-G2
E	[MPa]	10597.7	10610.4	10639.3
ν	[−]	0.343	0.343	0.343
$\mathbf{D_{11}}$	[MPa]	15370.8	15368.6	15363.8
$\mathbf{D_{33}}$	[MPa]	14153.3	14210.0	14337.2
$\mathbf{D_{13}}$	[MPa]	7892.9	7888.9	7879.9
$\mathbf{D_{55}}$	[MPa]	3123.9	3124.7	3126.3
$\mathbf{d_{33}}$	[mm/V]	3.73E-09	4.33E-09	5.32E-09
$\mathbf{d_{31}}$	[mm/V]	−1.80E-09	−2.09E-08	−2.57E-09
$\mathbf{d_{15}}$	[mm/V]	5.50E-09	6.39E-09	7.85E-09
$\boldsymbol{\kappa_3}$	[F/mm]	3.18E-10	3.18E-10	3.20E-10
$\boldsymbol{\kappa_1}$	[F/mm]	4.67E-10	4.67E-10	4.67E-10
$\boldsymbol{\kappa_3^{rel}}$	[−]	35.92	35.98	36.11
$\boldsymbol{\kappa_1^{rel}}$	[−]	52.73	52.74	52.77

field in the polarization direction, as the laminate deforms radially (Fig. 11). For this reason, the constants are varied keeping the same proportion of Eq. (31), until a good fit to the initial model (the one with only d_{33}) is reached. The results are shown in Table 11.

The resulting ratio between the experimental equivalent d_{33}^{eq} and the FE model d_{33}^{FE} is:

$$d_{33}^{eq} / d_{33}^{FE} = 0.733 \tag{32}$$

The updated properties for the PZT-powder composite comprising d_{31} and d_{15} are reported in Table 12.

6. Conclusions

A novel composite made from epoxy resin matrix and PZT powder particles has been simulated with a SVE approach in this work. The experiments from Gino et al. [32] are used as a reference to compare the results of the simulation with properties coming from the SVE.

An optical micrograph of the laminate cross-section is used as a geometry for a two-dimensional plane strain SVE of the composite. Three different sizes of the SVE are investigated, namely 0.15 mm, 0.3 mm and 0.5 mm. The effective elastic moduli are calculated as the relation between the average stresses and strain field produced by homogeneous boundary conditions. The dielectric constants are calculated knowing the electrostatic energy of the representative volume element. The piezoelectric deformation constant d_{33} is determined as the ratio of the strain to the electric field applied in the polarization direction.

The resulting properties are then implemented in finite element models of the sensing laminates, whose sensitivities are compared to the experimental ones.

The results show a comparable trend of sensitivity, which decreases as the distance between the electrodes increases. Nevertheless, the steepness of the sensitivity drop of the experimental samples is sharper. The sensitivity of the sample with the highest electrodes distance (P2400-G8, 8 GFRP plies between the electrodes) is captured with very good agreement regardless of the SVE size used for the retrieval of the homogenized moduli, dielectric, and piezoelectric constants. The properties derived from the SVE with 0.15 mm edge size are overall the best fit for the experimental curve, presumably due to the other SVEs being of comparable dimension with respect to the total thickness of the PZT-powder-resin composite. Overall, the proposed procedure for the prediction of the homogenized properties starting from the constituents is deemed to work properly.

It is also possible to evaluate the piezoelectric constants d_{31} and d_{15} that are not available experimentally, leading to the complete characterization of the PZT-epoxy layer.

The outcome of this work is therefore a complete characterization of the novel piezoelectric composite, for both mechanical and electrical properties, enabling the FE modeling of these types sensing laminates under any given loading scenario.

As a possible future endeavor, the manufacturing of a monodisperse PZT powder with smaller particle size could be useful not only for a better integration in the laminate, but also as a more convenient way to estimate the homogenized properties of the sensing layer.

CRediT authorship contribution statement

Michele Gulino: Writing – original draft, Methodology, Investigation, Formal analysis, Conceptualization. **Andrea Zucchelli:** Supervision, Project administration, Conceptualization. **Alessandro Pirondi:** Writing – original draft, Supervision, Project administration, Conceptualization. **Tommaso Brugo:** Supervision, Methodology, Investigation, Conceptualization.

Declaration of competing interest

The authors declare that they have no known competing financial interests or personal relationships that could have appeared to influence the work reported in this paper.

Data availability

Data will be made available on request.

Acknowledgements

This research was carried as part of the project DOT13SJY60, Ministerial Decree No. 1061 of August 10, 2021 and funded under the "Programma Operativo Nazionale" (PON), Action IV.4 "PhD grant on Innovation Thematics".

Appendix. – Piezoelectric behavior and coordinate transformation

The piezoelectric materials in this paper are assumed to display a linear piezoelectric behavior, that in an extended tensorial notation can be written as:

$$\varepsilon_{ij} = S_{ijhk}\sigma_{hk} + d_{nij}\Psi_n \tag{A.1}$$

$$\Delta_i = d_{ihk}\varepsilon_{hk} + \kappa_{in}\Psi_n \tag{A.2}$$

Where $\boldsymbol{\varepsilon}$, $\boldsymbol{S}$, $\boldsymbol{\sigma}$, $\boldsymbol{d}$, Ψ and Δ are the strain, compliance, stress, piezoelectric strain, electric field and electric displacement tensors.

With the same contracted notation introduced in this work, the constitutive matrix of the coupled electro-mechanical problem for an orthotropic material is:

$$\begin{bmatrix}\varepsilon_1\\ \varepsilon_2\\ \varepsilon_3\\ \varepsilon_4\\ \varepsilon_5\\ \varepsilon_6\\ \Delta_1\\ \Delta_2\\ \Delta_3\end{bmatrix} = \begin{bmatrix} S_{11} & S_{12} & S_{13} & 0 & 0 & 0 & 0 & 0 & d_{31}\\ S_{21} & S_{22} & S_{23} & 0 & 0 & 0 & 0 & 0 & d_{32}\\ S_{31} & S_{32} & S_{33} & 0 & 0 & 0 & 0 & 0 & d_{33}\\ 0 & 0 & 0 & S_{44} & 0 & 0 & 0 & 0 & 0\\ 0 & 0 & 0 & 0 & S_{55} & 0 & d_{15} & 0 & 0\\ 0 & 0 & 0 & 0 & 0 & S_{66} & 0 & d_{26} & 0\\ 0 & 0 & 0 & 0 & d_{15} & 0 & \kappa_1 & 0 & 0\\ 0 & 0 & 0 & 0 & 0 & d_{26} & 0 & \kappa_2 & 0\\ d_{31} & d_{32} & d_{33} & 0 & 0 & 0 & 0 & 0 & \kappa_3\end{bmatrix}\begin{bmatrix}\sigma_1\\ \sigma_2\\ \sigma_3\\ \sigma_4\\ \sigma_5\\ \sigma_6\\ \Psi_1\\ \Psi_2\\ \Psi_3\end{bmatrix} \tag{A.3}$$

For instance, the d_{15} constant, which in extended notation is d_{113} couples the electric field in the 1 direction (first subscript in d_{113}) and the subsequent angular deformation in the 13 plane, such as in Fig. A.1.

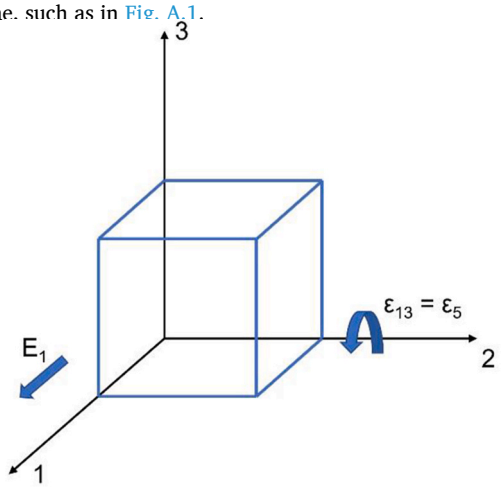

Fig. A.1. Piezoelectric d_{15} effect.

A change in the polarization direction from 3 to 2, leads to a rearrangement of the piezoelectric matrix such as:

$$\begin{bmatrix} 0 & 0 & 0 & 0 & d_{113} & 0\\ 0 & 0 & 0 & 0 & 0 & d_{223}\\ d_{311} & d_{322} & d_{333} & 0 & 0 & 0\end{bmatrix} \rightarrow \begin{bmatrix} 0 & 0 & 0 & d_{112} & 0 & 0\\ d_{211} & d_{222} & d_{233} & 0 & 0 & 0\\ 0 & 0 & 0 & 0 & 0 & d_{323}\end{bmatrix} \rightarrow \begin{bmatrix} 0 & 0 & 0 & d_{14} & 0 & 0\\ d_{21} & d_{22} & d_{23} & 0 & 0 & 0\\ 0 & 0 & 0 & 0 & 0 & d_{36}\end{bmatrix} \tag{A.4}$$

References

[1] C. Maierhofer, P. Myrach, M. Reischel, H. Steinfurth, M. Röllig, M. Kunert, Characterizing damage in CFRP structures using Flash thermography in reflection and transmission configurations, Compos. B Eng. 57 (2014) 35–46, https://doi.org/10.1016/j.compositesb.2013.09.036.

[2] D.J. Bull, S.M. Spearing, I. Sinclair, L. Helfen, Three-dimensional assessment of low velocity impact damage in particle toughened composite laminates using micro-focus X-ray computed tomography and synchrotron radiation laminography, Compos. Appl. Sci. Manuf. 52 (2013) 62–69, https://doi.org/10.1016/j.compositesa.2013.05.003.

[3] D.G. Aggelis, A.C. Mpalaskas, T.E. Matikas, D. Van Hemelrijck, Acoustic emission signatures of damage modes in structural materials, in: Nondestructive Characterization for Composite Materials, Aerospace Engineering, Civil Infrastructure, and Homeland Security, 2013, SPIE, 2013, p. 86940T, https://doi.org/10.1117/12.2008942.

[4] J. Cai, L. Qiu, S. Yuan, L. Shi, P. Liu, D. Liang, Structural health monitoring for composite materials, in: Composites and Their Applications, InTech, 2012, https://doi.org/10.5772/48215.

[5] H. Chen, Y. Ni, Structural Health Monitoring of Large Civil Engineering Structures, Wiley, 2018, https://doi.org/10.1002/9781119166641.

[6] Y. Chen, X. Xue, Advances in the structural health monitoring of bridges using piezoelectric transducers, Sensors 18 (12) (2018), https://doi.org/10.3390/s18124312. MDPI AG.

[7] D.E. Adams, Health Monitoring of Structural Materials and Components, Wiley, 2007, https://doi.org/10.1002/9780470511589.

[8] M.E. Voutetaki, M.C. Naoum, N.A. Papadopoulos, C.E. Chalioris, Cracking diagnosis in fiber- reinforced concrete with synthetic fibers using piezoelectric transducers, Fibers 10 (1) (2022), https://doi.org/10.3390/fib10010005.

[9] D.G. Aggelis, A.C. Mpalaskas, T.E. Matikas, Acoustic monitoring for the evaluation of concrete structures and materials, in: Acoustic Emission (AE) and Related Non-destructive Evaluation (NDE) Techniques in the Fracture Mechanics of Concrete: Fundamentals and Applications, Elsevier Inc., 2015, pp. 269–286, https://doi.org/10.1016/B978-1-78242-327-0.00013-1.

[10] M. Naoum, G. Sapidis, N. Papadopoulos, E. Golias, C.E. Chalioris, Structural health monitoring of reinforced concrete beam-column joints using piezoelectric transducers, in: International RILEM Conference on Synergising Expertise towards Sustainability and Robustness of CBMs and Concrete Structures, Springer Nature Switzerland, 2023, pp. 945–956, https://doi.org/10.1007/978-3-031-33211-1_85.

[11] D. Cristiani, F. Falcetelli, N. Yue, C. Sbarufatti, R. Di Sante, D. Zarouchas, M. Giglio, Strain-based delamination prediction in fatigue loaded CFRP coupon specimens by deep learning and static loading data, Compos. B Eng. 241 (2022), https://doi.org/10.1016/j.compositesb.2022.110020.

[12] J.M. López-Higuera, L.R. Cobo, A.Q. Incera, A. Cobo, Fiber optic sensors in structural health monitoring, J. Lightwave Technol. 29 (4) (2011) 587–608, https://doi.org/10.1109/JLT.2011.2106479.

[13] M.S.M. Desa, M.H.W. Ibrahim, S. Shahidan, N.S. Ghadzali, Z. Misri, Fundamental and assessment of concrete structure monitoring by using acoustic emission technique testing: a review, in: IOP Conference Series: Earth and Environmental Science, Institute of Physics Publishing, Apr. 2018, https://doi.org/10.1088/1755-1315/140/1/012142.

[14] H. Choi, S. Choi, H. Cha, Structural health monitoring system based on strain gauge enabled Wireless sensor nodes, in: 2008 5th International Conference on Networked Sensing Systems, 2008, pp. 211–214.

[15] H. Mei, M.F. Haider, R. Joseph, A. Migot, V. Giurgiutiu, Recent advances in piezoelectric wafer active sensors for structural health monitoring applications, Sensors 19 (2) (Jan. 2019), https://doi.org/10.3390/s19020383.

[16] B.Y. Mohammed, C.K. Tan, S.J. Wilcox, A.Z.S. Chong, Damage characterisation of carbon fibre reinforced composite plate using acoustic emission, in: Key Engineering Materials, Trans Tech Publications Ltd, 2013, pp. 184–194. https://doi.org/10.4028/www.scientific.net/KEM.558.184.

[17] Q. Wu, Y. Okabe, F. Yu, Ultrasonic structural health monitoring using fiber bragg grating, Sensors 18 (10) (2018), https://doi.org/10.3390/s18103395. MDPI AG.

[18] S. Jinachandran, G. Rajan, Fibre bragg grating based acoustic emission measurement system for structural health monitoring applications, Materials 14 (4) (2021) 1–16, https://doi.org/10.3390/ma14040897.

[19] Y. Meyer, R. Lachat, G. Akhras, A review of manufacturing techniques of smart composite structures with embedded bulk piezoelectric transducers, Smart Mater. Struct. 28 (5) (2019), https://doi.org/10.1088/1361-665X/ab0fab. Institute of Physics Publishing.

[20] M. Kulkarni, D. Carnahan, K. Kulkarni, D. Qian, J.L. Abot, Elastic response of a carbon nanotube fiber reinforced polymeric composite: a numerical and

experimental study, Compos. B Eng. 41 (5) (2010) 414–421, https://doi.org/10.1016/j.compositesb.2009.09.003.
[21] J.L. Abot, Y. Song, M.S. Vatsavaya, S. Medikonda, Z. Kier, C. Jayasinghe, N. Rooy, V.N. Shanov, M.J. Schulz, Delamination detection with carbon nanotube thread in self-sensing composite materials, Compos. Sci. Technol. 70 (7) (2010) 1113–1119, https://doi.org/10.1016/j.compscitech.2010.02.022.
[22] J.J. Ku-Herrera, F. Avilés, G.D. Seidel, Self-sensing of elastic strain, matrix yielding and plasticity in multiwall carbon nanotube/vinyl ester composites, Smart Mater. Struct. 22 (8) (2013), https://doi.org/10.1088/0964-1726/22/8/085003.
[23] T.M. Brugo, E. Maccaferri, D. Cocchi, L. Mazzocchetti, L. Giorgini, D. Fabiani, A. Zucchelli, Self-sensing hybrid composite laminate by piezoelectric nanofibers interleaving, Compos. B Eng. 212 (2021), https://doi.org/10.1016/j.compositesb.2021.108673.
[24] G. Selleri, M.E. Gino, T.M. Brugo, R. D'Annibale, J. Tabucol, M.L. Focarete, R. Carloni, D. Fabiani, A. Zucchelli, Self-sensing composite material based on piezoelectric nanofibers, Mater. Des. 219 (2022), https://doi.org/10.1016/j.matdes.2022.110787.
[25] W. Du, J. Hoyt, N. Williams, K.A. Cook-Chennault, The influence of processing parameters on piezoelectric and dielectric properties of Dome-Shaped composite PZT-epoxy actuators, J. Manuf. Process. 57 (2020) 48–60, https://doi.org/10.1016/j.jmapro.2020.05.036.
[26] I. Payo, J.M. Hale, Dynamic characterization of piezoelectric paint sensors under biaxial strain, Sensor Actuator Phys. 163 (1) (2010) 150–158, https://doi.org/10.1016/j.sna.2010.08.005.
[27] N.K. James, D. van den Ende, U. Lafont, S. van der Zwaag, W.A. Groen, Piezoelectric and mechanical properties of structured PZT–epoxy composites, J. Mater. Res. 28 (4) (2013) 635–641, https://doi.org/10.1557/jmr.2012.428.
[28] J. Khaliq, D.B. Deutz, J.A.C. Frescas, P. Vollenberg, T. Hoeks, S. van der Zwaag, P. Groen, Effect of the piezoelectric ceramic filler dielectric constant on the piezoelectric properties of PZT-epoxy composites, Ceram. Int. 43 (2) (2017) 2774–2779, https://doi.org/10.1016/j.ceramint.2016.11.108.
[29] S. Egusa, N. Iwasawa, Application of piezoelectric paints to damage detection in structural materials, J. Reinforc. Plast. Compos. 15 (8) (1996) 806–817, https://doi.org/10.1177/073168449601500804.
[30] S. Egusa, N. Iwasawa, Piezoelectric paints: preparation and application as built-in vibration sensors of structural materials, J. Mater. Sci. 28 (6) (1993) 1667–1672, https://doi.org/10.1007/BF00363366.
[31] J.M. Hale, J. Tuck, A novel thick-film strain transducer using piezoelectric paint, Proc. IME C J. Mech. Eng. Sci. 213 (6) (1999) 613–622, https://doi.org/10.1243/0954406991522545.
[32] M.E. Gino, G. Selleri, D. Cocchi, T.M. Brugo, N. Testoni, L. De Marchi, A. Zucchelli, D. Fabiani, M.L. Focarete, On the design of a piezoelectric self-sensing smart composite laminate, Mater. Des. 219 (2022) 110783, https://doi.org/10.1016/j.matdes.2022.110783.
[33] Z. Hashin, Elasticity of random media, Trans. Soc. Rheol. 9 (1) (1965) 381–406, https://doi.org/10.1122/1.549014.
[34] J. Aboudi, Mechanics of Composite Materials - A Unified Micromechanical Approach, Elsevier, 1991.
[35] R. Hill, Elastic properties of reinforced solids: some theoretical principles, J. Mech. Phys. Solid. (1963) 357–372.
[36] R. Hill, A self-consistent mechanics of composite materials, J. Mech. Phys. Solid. 13 (1965) 213–222.
[37] Z.F. Khisaeva, M. Ostoja-Starzewski, On the size of RVE in finite elasticity of random composites, J Elast 85 (2) (Nov. 2006) 153–173, https://doi.org/10.1007/s10659-006-9076-y.
[38] M. Ostoja-Starzewski, Material spatial randomness: from statistical to representative volume element, Probabilist. Eng. Mech. 21 (2) (Apr. 2006) 112–132, https://doi.org/10.1016/j.probengmech.2005.07.007.
[39] M. Pingaro, M.L. De Bellis, E. Reccia, P. Trovalusci, T. Sadowski, Fast statistical homogenization procedure for estimation of effective properties of ceramic matrix composites (CMC) with random microstructure, Compos. Struct. 304 (Jan. 2023), https://doi.org/10.1016/j.compstruct.2022.116265.
[40] I.S. Abbood, S.A. Odaa, K.F. Hasan, M.A. Jasim, Properties evaluation of fiber reinforced polymers and their constituent materials used in structures - a review, in: Materials Today: Proceedings, Elsevier Ltd, 2021, pp. 1003–1008, https://doi.org/10.1016/j.matpr.2020.07.636.
[41] Q. Dai, K. Ng, Investigation of electromechanical properties of piezoelectric structural fiber composites with micromechanics analysis and finite element modeling, Mech. Mater. 53 (2012) 29–46, https://doi.org/10.1016/j.mechmat.2012.04.014.
[42] G.M. Odegard, Constitutive modeling of piezoelectric polymer composites, Acta Mater. 52 (18) (2004) 5315–5330, https://doi.org/10.1016/j.actamat.2004.07.037.
[43] X. Xu, B. Zhang, K. Liu, D. Liu, M. Bai, Y. Li, Finite element simulation and analysis of the dielectric properties of unidirectional aramid/epoxy composites, Polym. Compos. 39 (2018) E2226–E2233, https://doi.org/10.1002/pc.24586.
[44] Y. Lin, H.A. Sodano, A double inclusion model for multiphase piezoelectric composites, Smart Mater. Struct. 19 (3) (2010), https://doi.org/10.1088/0964-1726/19/3/035003.
[45] M. Stewart, M.G. Cain, Direct Piezoelectric Measurement: the Berlincourt Method, 2014, pp. 37–64, https://doi.org/10.1007/978-1-4020-9311-1_3.
[46] M. Stewart, W. Battrick, M. Cain, Measurement Good Practice Guide No. 44 - Measuring Piezoelectric D33 Coefficients Using the Direct Method, 2001.